Available online at www.sciencedirect.com
SCIENCE DIRECT®
International Journal of Multiphase Flow 32 (2006) 692–716
International Journal of Multiphase Flow
www.elsevier.com/locate/ijmulflow

Effect of feedback and inter-particle collisions in an idealized gas–liquid annular flow

Yoichi Mito, Thomas J. Hanratty *

Department of Chemical and Biomolecular Engineering, University of Illinois, 205 Roger Adams Laboratory, Box C-3, 600 South Mathews Avenue, Urbana, IL 61801, USA

Received 18 July 2005; received in revised form 6 February 2006

Abstract

An idealized gas–liquid annular flow in a vertical rectangular channel was considered. Point sources of solid spheres were located on the walls to represent an atomizing wall film. The decrease in the deposition coefficient with increasing volume fraction, observed in laboratory studies, was examined by using a direct numerical simulation, which does not fully resolve scales of the size of particles, to calculate the fluid turbulence. The influence of particles on the fluid turbulence was modeled simply by introducing point forces at particle loci. Inter-particle collisions were also considered. Significant attenuation of fluid turbulence at very low concentrations could be observed as resulting from the feedback effect of particles. In the fluid momentum balance the fluid Reynolds shear stresses decrease with increasing the volume fraction in order to accommodate the particle forces. This leads to a decrease in the production of fluid turbulence and, therefore, to a decrease in particle turbulence. Particle turbulence is augmented by elastic inter-particle collisions and can be attenuated by inelastic inter-particle collisions. The decrease in the deposition coefficient, observed in gas–liquid annular flows, can be explained by the feedback effect if droplet collisions are highly inelastic. When feedback and elastic inter-particle collisions are considered, changes in the particle turbulence are mainly associated with elastic inter-particle collisions at large enough volume fractions.

The observed influence of point forces on fluid turbulence has a kinship to findings on polymer drag reduction in that polymer molecules (or aggregates) create local stresses in the fluid and the Reynolds shear stresses decrease to accommodate these polymer stresses.

Keywords: Gas–liquid annular flow; Dispersed flow; Feedback effect; Inter-particle collisions; Particle deposition; Direct numerical simulation

1. Introduction

The annular pattern for gas–liquid flows is dominant in many applications. Part of the liquid flows as a film along the wall and part is entrained as drops in a high speed gas flow. A liquid exchange exists whereby the

* Corresponding author. Tel.: +1 217 333 1318; fax: +1 217 333 5052.
E-mail address: hanratty@scs.uiuc.edu (T.J. Hanratty).

0301-9322/$ - see front matter
doi:10.1016/j.ijmultiphaseflow.2006.02.007

film is atomized and drops are deposited on the film. Usual practice is to assume that the rate of deposition, R_D, varies linearly with the bulk concentration of drops, C_B:

$$R_D = k_{DB} C_B = k_{DB} \rho_p \alpha, \tag{1}$$

where k_{DB} is the deposition coefficient, ρ_p is the density of the particles and α is the volume fraction. The deposition coefficient is found to be approximated as $k_{DB} = \sigma_p/\sqrt{2\pi}$, where σ_p is the root mean square of the wall-normal velocity fluctuations of the drops at a location just outside the viscous wall layer (Hay et al., 1996).

Measurements of R_D by Schadel et al. (1990) and by Govan et al. (1988), as well as earlier measurements by Namie and Ueda (1972) and by Andreussi and Zanelli (1976), show that k_{DB} decreases dramatically with increasing α (or C_B) at large α. Fig. 1 presents laboratory measurements of R_D by Schadel et al. (1990) for upflow of air and water in a 2.54 cm pipe and by Andreussi (1983) for downflow of air and water in a 2.4 cm pipe. These are characterized by a rate of deposition that varies linearly with α at small α and that is roughly constant at large α, that is, a constant value of k_{DB} at small α and an α^{-1} variation at large α. The usual explanations for the observed decreases in k_{DB} are that the fluid turbulence is damped (Namie and Ueda, 1972) or that drop interactions are occurring (Teixeira et al., 1987; Hay et al., 1996). Experiments by Hay et al. (1996) showed that changes in k_{DB} could not be explained by changes in the diameters of the drops along the pipe. Furthermore, measurements of mean fluid velocity profiles seem to suggest that fluid turbulence was not decreasing. (We will show that this agreement need not indicate the absence of changes in fluid turbulence.) They, therefore, supported the notion that the decrease in k_{DB} was due to drop encounters. To a large extent, the exploration of this explanation motivated our research.

The present paper presents results of a study of the suspension associated with an idealized annular flow described in the next section. A direct numerical simulation which does not resolve scales of the size of the particles is used. The influence of particles on fluid turbulence is simply represented by introducing point forces at particle loci. This is the "point force method" used in several previous investigations. The particle turbulence and, therefore, the deposition coefficient tend to decrease with decreases in fluid turbulence. However, particle turbulence is also affected by collisions. The effects of particle collisions were studied by solving the equation of motion of particles entrained in the DNS.

The two main contributions are (1) the provision of an explanation of the results in Fig. 1 and (2) an examination of the point force method as a means to represent feedback.

A calculation in which the fluid turbulence is represented by a stochastic model is presented in Appendix A. This fails to capture all of the effects seen in the DNS used in this study and points out the need to capture small-scale fluid turbulence, particularly when considering particle collisions. Four types of studies were made in the DNS: (1) a calculation with no feedback and no inter-particle collisions (one-way coupling), (2) calculations with only feedback (two-way coupling), (3) calculations with only elastic or inelastic inter-particle collisions and (4) calculations with both feedback and inter-particle collisions (four-way coupling).

The damping of fluid turbulence in the presence of a very dilute concentration of solid particles has received the attention of a number of investigators in recent years. Kulick et al. (1994) used laser-Doppler techniques to study fluid and solid turbulence in a dilute dispersed downward flow in a channel. Particles with dimensionless

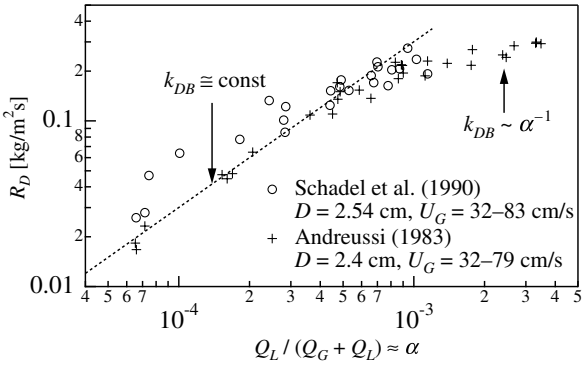

Fig. 1. Rate of deposition in gas–liquid annular flows.

inertial time constants of $\tau_p^+ = 300$ and $\tau_p^+ = 2100$ were used. They found that fluid turbulence decreased with increasing volume fraction of solid spheres but that the profile of mean fluid velocities was unchanged. Similar results were obtained by Paris and Eaton (2001), who used particle-image velocimetry to study a dispersed flow of solid spheres, with $\tau_p^+ = 2600$, in a vertical channel. Segura et al. (2004) used a point force method in a large eddy simulation (LES) to calculate the effect of feedback in the experiments performed by Paris and Eaton (2001). An attenuation of turbulence of the magnitude observed in laboratory experiments was not calculated. This could suggest an inadequacy of the point force method to calculate feedback effects. However, Li et al. (2001) found significant effects of feedback for a suspension of particles, with $\tau_p^+ = 190$, by using the point force method in a DNS.

Yamamoto et al. (2001) examined the effects of inter-particle collisions for dispersed flows of particles with $\tau_p^+ = 27$, 1000, 2100 in a vertical channel. They used LES and the point force method to calculate the fluid velocity field seen by the particles. Li et al. (2001) included the effect of collisions in their DNS experiments. They focussed mainly on collisions that are elastic or slightly inelastic.

2. Idealized annular flow

The idealized representation of an annular flow in a rectangular channel used in this study is described by Mito and Hanratty (2004b). The rectangular channel has a height of $2H$ and is infinitely wide. Gas is flowing through the channel turbulently at a constant rate. The Reynolds number, Re_b, defined with the bulk mean velocity and the half-height of the channel, H, is 2260. The Reynolds number, Re_τ, defined with the friction velocity in the absence of particles, v_0^*, and H is 150. Cartesian coordinates x_1, x_2 and x_3 are assigned to the streamwise, wall-normal and spanwise directions. The channel walls are located at $x_2 = 0$ and $x_2 = 2H$ and are considered to be the loci of instantaneous sources of particles. Periodicity is assumed in the x_1 and x_3 directions.

Droplets are represented by solid spheres with a dimensionless diameter of $d_p^+ = d_p v_0^*/v = 1.9$ and a density ratio of $\rho_p/\rho_f = 1000$, for which the dimensionless Stokesian inertial time constant is $\tau_p^+ = d_p^{+2}(\rho_p/\rho_f)/18 = 200$, where ρ_p is the density of the particle and ρ_f is the density of the fluid. This τ_p^+ was chosen as representative of the annular flow regime (Mito and Hanratty, 2004b) and is nearly equal to the time constant characterizing the solid particles used in the studies of Li et al. (2001). (The particle size, $d_p^+ = 1.9$, was fixed after the choice of τ_p^+ and the density ratio for gas–liquid flow, $\rho_p/\rho_f = 1000$.) Gravity is assumed to be zero, so the results can be best applied to vertical flows.

Woodmansee and Hanratty (1969) have shown that atomization of wall films occurs by a rapid growth and removal of capillary waves which create drops that are entrained by the gas turbulence in the region outside the viscous wall layer. This would suggest that, in the absence of more data, drops should be placed in the field at a short distance from the wall with a velocity characteristic of the mean velocity and the root mean square of the velocity fluctuations just outside the viscous wall layer. This process is modeled by injecting the particles from $x_2 = d_p/2$ with a velocity of $(15v_0^*, v_0^*, 0)$ and a rate per unit area of R_{Ib}. The particles are also injected from $x_2 = 2H - d_p/2$ with a velocity of $(15v_0^*, -v_0^*, 0)$ and a rate per unit area of R_{It}. The coordinates on a wall, x_1 and x_3, from which particles are injected are randomly selected. The particles are removed from the field when they hit a wall. Thus, the analysis differs from most previous computer simulations which allow the particles to bounce from the wall.

Effects of changes in the injection velocity or in d_p^+ on the rate of deposition for the idealized annular flow were discussed by Mito and Hanratty (2004a). Increases in the injection velocity have the effect of placing the particles at a larger distance from the wall before they start to mix due to turbulence. The effects of changes in the injection velocity were found to be negligibly small. Changes in d_p^+ affect the concentration field and the rate of deposition because τ_p^+ and the distance of the particle center from the wall at deposition change. The effects of changes in d_p^+ are mainly associated with changes in τ_p^+ for the annular flow regime because of the large contribution of particles in free-flights.

The calculation is done by injecting particles from both walls, with fixed rates, into the single-phase fully developed turbulent flow. The rates of injection are the same at both walls, $R_{Ib} = R_{It} = R_I$, because of the symmetry of the system. The calculation is carried out until a statistically stationary state, for which the concentration of particles is such that the rates of injection and deposition are the same at both walls and the mean

wall-normal particle velocities are zero at all x_2. Disperse flows with various volume fractions are realized by varying the rate of injection. In this study, the number of the particles injected from an area, $1900v/v_0^* \times 950v/v_0^*$, per time step, $\Delta t^+ = \Delta t v_0^{*2}/v = 0.25$, is varied from 0.1 to 50. (The volume fraction at a stationary state in this type of simulation is not known a priori.) It was found there is a critical R_I above which a stationary state is not reached and particle concentration continues to increase with time. Results for non-stationary cases are also presented.

3. Theoretical considerations

3.1. Feedback effect

Particles have been observed to affect the fluid turbulence even with volume fractions of $O(10^{-5})$ (Elghobashi and Truesdell, 1993). The feedback effect of particles on fluid flow has been modeled with a point force method using the assumption that the particles are small enough that eddy shedding does not occur (Crowe et al., 1977). Squire and Eaton (1990) and Elghobashi and Truesdell (1993) used this approach in a DNS of an isotropic field and Pan and Banerjee (1996) and Li et al. (2001), in a DNS of a turbulent flow through a channel.

Trajectories of small spherical particles are calculated with the following equations:

$$\frac{\mathrm{d}x_i}{\mathrm{d}t} = V_i, \tag{2}$$

$$\frac{\mathrm{d}V_i}{\mathrm{d}t} = -\frac{3\rho_\mathrm{f} C_\mathrm{D}}{4 d_\mathrm{p} \rho_\mathrm{p}} |\boldsymbol{V} - \boldsymbol{U}|(V_i - U_i) = f_{\mathrm{p}i}, \tag{3}$$

where V_i is the velocity of the particle, U_i is the fluid velocity seen by the particle, ρ_p is the density of the particle, ρ_f is the density of the fluid, and C_D is the drag coefficient, which is given by

$$C_\mathrm{D} = \frac{24}{Re_\mathrm{p}}\left(1 + 0.15 Re_\mathrm{p}^{0.687}\right), \tag{4}$$

where the particle Reynolds number, Re_p, is defined with d_p and the magnitude of the relative velocity, $|\boldsymbol{V} - \boldsymbol{U}|$. Because of the assumption of a large density ratio, $\rho_\mathrm{p}/\rho_\mathrm{f} = 1000$, the lift force is ignored in Eq. (3).

The force of particles on the fluid motion at a grid point is represented as the sum of the reaction forces exerted by the particles whose centers exist in the computational cell surrounding the grid point (Li et al., 2001):

$$F_i = -\frac{\rho_\mathrm{p}}{\rho_\mathrm{f}} \frac{V_\mathrm{p}}{V_\mathrm{cell}} \sum_{k=1}^{N_\mathrm{cell}} f_{\mathrm{p}ik} = -\frac{C}{\rho_\mathrm{f}} \langle f_{\mathrm{p}i} \rangle_\mathrm{cell}, \tag{5}$$

where a monodisperse flow ($d_\mathrm{p} = \text{constant}$) is assumed, $V_\mathrm{p} (= \pi d_\mathrm{p}^3/6)$ is the volume of a particle, V_cell is the volume of the computational cell, N_cell is the number of particles in the cell, $f_{\mathrm{p}ik}$ is the $f_{\mathrm{p}i}$ defined by Eq. (3) for the kth particle, $C = \rho_\mathrm{p} V_\mathrm{p} N_\mathrm{cell}/V_\mathrm{cell}$ is the concentration of particles and $\langle f_{\mathrm{p}i} \rangle_\mathrm{cell}$ is the average point force of the N_cell particles. (Thus the reaction force exerted by a particle is considered in a single computational cell even when the particle exists across multiple cells. Then the numerical effective size of a particle is the size of the computational cell in which the center of the particle exists.) The fluid phase is assumed to be incompressible ($\rho_\mathrm{f} = \text{constant}$). Then the Navier–Stokes equation is given as

$$\rho_\mathrm{f}\left(\frac{\partial U_i}{\partial t} + U_j \frac{\partial U_i}{\partial x_j}\right) = -\frac{\partial P}{\partial x_i} + \mu \frac{\partial^2 U_i}{\partial x_j \partial x_j} + \rho_\mathrm{f} F_i, \tag{6}$$

where $\partial P/\partial x_i$ is a component of the pressure gradient and $\mu = \rho_\mathrm{f} v$ is the coefficient of viscosity of the fluid.

3.2. Inter-particle collision

Inter-particle collisions also have been observed to affect the particle turbulence with volume fractions of $O(10^{-3})$. These effects have been calculated in a Lagrangian framework with a deterministic method (Tanaka

and Tsuji, 1991; Lun and Liu, 1997; Li et al., 2001; Yamamoto et al., 2001) and with a stochastic method (Oesterle and Petitjean, 1993; Sommerfeld, 2001). The latter needs to be modified in, as yet, an undefined way, when it is used for inhomogeneous turbulence. In this study, a deterministic approach was used. The detection method for inter-particle collisions, described by Chen et al. (1998) and Li et al. (2001), was used. The volume fraction is small enough that only binary collisions need to be considered. The effect of the fluid on colliding particles is neglected during the time step, in which collision occurs, on the assumption that the effect of the impact is dominant.

Rotation of colliding particles is known to affect the trajectories of the particles after the collision (Lun and Savage, 1987). However, many uncertainties exist in the calculation of the angular velocity of a particle on its trajectory. Therefore, in the calculations, rotation of a particle is assumed to be zero on its trajectory and when inter-particle collisions are occurring. A collision occurs between two spherical particles, 1 and 2, with equal diameters. The changes of velocities, $\boldsymbol{V}_1$ and $\boldsymbol{V}_2$, are described by

$$\boldsymbol{k}\cdot\left(\boldsymbol{V}_1'-\boldsymbol{V}_2'\right)=-e\boldsymbol{k}\cdot(\boldsymbol{V}_1-\boldsymbol{V}_2), \tag{7}$$

$$\boldsymbol{k}\times\left(\boldsymbol{V}_1'-\boldsymbol{V}_2'\right)=-\beta\boldsymbol{k}\times(\boldsymbol{V}_1-\boldsymbol{V}_2), \tag{8}$$

where $\boldsymbol{V}_1'$ and $\boldsymbol{V}_2'$ are the velocities of the particles after the collision, $\boldsymbol{k}$ is the unit vector along the center line from particle 1 to particle 2, e is the coefficient of restitution and β is the roughness coefficient (Lun and Savage, 1987). We test two types of collision models: (1) an elastic model, for which $e=1$ and $\beta=-1$, (2) inelastic models, for which the relative tangential velocity of particles after a collision is assumed to be zero, that is, $\beta=0$ (Campbell and Brennen, 1985) and several coefficients of restitution, 0, 0.1, 0.4, 0.7, 1, are considered. Interactions of droplets are thought to be inelastic, so the calculations with elastic inter-particle collisions give limiting behaviors for the gas–liquid annular flow. Furthermore, they allow an examination of similarities with previous studies for disperse flows of solid particles.

The occurrence of inter-particle collisions is examined by calculating the trajectories of particles during a time step with a first-order Euler explicit method. A three-dimensional equispaced $95\times30\times96$ lattice that is set in the channel is used to restrict the volume in which a search of intersections of trajectories (Chen et al., 1998; Li et al., 2001) is made. The searching volume for each particle is the cell in which the considered particle exists plus its surrounding 26 cells (17 cells when the considered particle exists in a cell attached to a wall). The dimensions of each cell are $20\nu/v_0^*$, $10\nu/v_0^*$, $10\nu/v_0^*$ in the x_1, x_2, x_3 directions. These are large enough to capture the trajectories of a pair of colliding particles during the time step $\Delta t^+=0.25$.

3.3. Momentum balance in the fluid phase

In this section, the momentum balance in the fluid phase is considered. It is represented by an ensemble average of the Navier–Stokes equation

$$\rho_{\mathrm{f}}\left[\frac{\partial\overline{U}_i}{\partial t}+\frac{\partial}{\partial x_j}\left(\overline{U}_j\overline{U}_i+\overline{u_ju_i}\right)\right]=-\frac{\partial\overline{P}}{\partial x_i}+\mu\frac{\partial^2\overline{U}_i}{\partial x_j\partial x_j}+\rho_{\mathrm{f}}\overline{F}_i, \tag{9}$$

where u_i is the fluctuating component of U_i. An integration of the streamwise component of Eq. (9) from x_2 to H (where the Reynolds stress is zero because of symmetry) gives

$$-\frac{\partial\overline{P}}{\partial x_1}(H-x_2)=-\rho_{\mathrm{f}}\overline{u_1u_2}+\mu\frac{\partial\overline{U}_1}{\partial x_2}-\rho_{\mathrm{f}}\int_{x_2}^{H}\overline{F}_1(x_2)\,\mathrm{d}x_2. \tag{10}$$

At the wall ($x_2=0$), $\overline{u_1u_2}=0$, and $\mu(\partial\overline{U}_1/\partial x_2)$ is designated as $\bar{\tau}_{\mathrm{W}}$, so Eq. (10) gives the pressure drop as the sum of two terms

$$-\frac{\partial\overline{P}}{\partial x_1}=\frac{\bar{\tau}_{\mathrm{W}}}{H}-\rho_{\mathrm{f}}F_{1\mathrm{B}}, \tag{11}$$

where $F_{1\mathrm{B}}$ is the bulk mean streamwise point force, which is obtained by taking an ensemble average of Eq. (5); that is,

$$F_{1B} = \frac{1}{H}\int_0^H \overline{F}_1(y)\,dy = -\frac{\rho_p}{\rho_f}\frac{V_p}{V_c}N_B f_{p1B} = -\frac{C_B}{\rho_f}f_{p1B}, \tag{12}$$

where N_B is the average number of particles in V_c, the channel volume, f_{p1B} is the average of f_{p1} for all the particles and $C_B = \rho_p V_p N_B/V_c$ is the bulk concentration. It is noted in Eq. (11) that a positive value of F_{1B} contributes to a decrease in the magnitude of the pressure drop, which is defined as $-(\partial\overline{P}/\partial x_1)$.

3.4. Momentum balance in the solid phase

A momentum balance in the solid phase is

$$\frac{\partial CV_i}{\partial t} + \frac{\partial CV_jV_i}{\partial x_j} = Cf_{pi}. \tag{13}$$

For a fully developed flow in a channel, an ensemble average of Eq. (13) gives

$$\frac{\partial}{\partial x_2}\overline{C}\overline{v_2v_i} = \overline{C}\bar{f}_{pi}, \tag{14}$$

where v_i is the fluctuating component of V_i and $\overline{v_2v_i}$, $\bar{f}_{pi}$ are concentration weighted averages. For a symmetric field, an integration of Eq. (14) from $y = x_2$ to the channel center, $y = H$, gives

$$-\overline{C}\overline{v_1v_2} = \int_{x_2}^H \overline{C}\bar{f}_{p1}\,dy = -\rho_f\int_{x_2}^H \overline{F}_1\,dy, \tag{15}$$

where the ensemble average of the streamwise component of Eq. (5), $\rho_f\overline{F}_1 = -\overline{C}\bar{f}_{p1}$, is used. Eq. (15) shows that the integral of the particle force term may be considered to represent a particle Reynolds shear stress. By substituting Eq. (15) into Eq. (10), a relation for the fluid Reynolds shear stress is derived as

$$-\rho_f\overline{u_1u_2} = -\frac{\partial\overline{P}}{\partial x_1}(H - x_2) - \mu\frac{\partial\overline{U}_1}{\partial x_2} + \overline{C}\overline{v_1v_2}. \tag{16}$$

Eq. (15) at the wall ($x_2 = 0$) gives the momentum flux of the solid phase to the wall, that is,

$$-\overline{C}_W(\overline{v_1v_2})_W = C_B f_{p1B}H = -\rho_f F_{1B}H. \tag{17}$$

Thus, when $-(\overline{v_1v_2})_W < 0$ ($f_{1B} < 0$ and $F_{1B} > 0$) the particles are, on average, supplying streamwise momentum to the fluid. When $-(\overline{v_1v_2})_W > 0$ ($f_{1B} > 0$ and $F_{1B} < 0$) the particles are, on average, extracting streamwise momentum from the fluid. In the former case the momentum supplied by particles contributes to a decrease in the pressure drop, which is shown by substituting Eq. (17) into Eq. (11):

$$-\frac{\partial\overline{P}}{\partial x_1} = \frac{1}{H}\left[\bar{\tau}_W - \overline{C}_W(\overline{v_1v_2})_W\right]. \tag{18}$$

The pressure gradient is the sum of components representing molecular momentum transfer to the wall and net momentum transfer due to particle injection and deposition. Thus it is possible to have a decrease in drag, $\bar{\tau}_W$, and an increase in $-\partial\overline{P}/\partial x_1$ if $-(\overline{v_1v_2})_W > 0$.

3.5. Balance equation for fluid Reynolds stresses

The balance equation for fluid Reynolds stresses, when feedback is modeled with the point force method, is given as

$$\frac{\partial}{\partial t}\overline{u_iu_j} + \overline{U}_k\frac{\partial}{\partial x_k}\overline{u_iu_j} = P_{ij} + T_{ij} + \Pi_{ij} + D_{ij} + \varepsilon_{ij} + \mathrm{VPF}_{ij}, \tag{19a}$$

where

$$P_{ij} = -\left(\overline{u_i u_k}\frac{\partial \overline{U}_j}{\partial x_k} + \overline{u_j u_k}\frac{\partial \overline{U}_i}{\partial x_k}\right): \quad \text{Production}, \tag{19b}$$

$$T_{ij} = -\frac{\partial}{\partial x_k}\overline{u_i u_j u_k}: \quad \text{Turbulent transport}, \tag{19c}$$

$$\Pi_{ij} = -\frac{1}{\rho_f}\left(\overline{u_i\frac{\partial p}{\partial x_j}} + \overline{u_j\frac{\partial p}{\partial x_i}}\right): \quad \text{Velocity pressure-gradient correlation}, \tag{19d}$$

$$D_{ij} = \nu\frac{\partial^2}{\partial x_k^2}\overline{u_i u_j}: \quad \text{Viscous diffusion}, \tag{19e}$$

$$\varepsilon_{ij} = -2\nu\overline{\frac{\partial u_i}{\partial x_k}\frac{\partial u_j}{\partial x_k}}: \quad \text{Dissipation}, \tag{19f}$$

$$\mathrm{VPF}_{ij} = \overline{u_i f_j} + \overline{u_j f_i}: \quad \text{Velocity-point force correlation}, \tag{19g}$$

where f_i is the fluctuating component of the point force, F_i. The left side of Eq. (19a) is zero for a statistically stationary case in the system being considered. It is noted that direct contributions of particle forces to the transport of the fluid Reynolds stresses are represented by the velocity-point force correlation shown as Eq. (19g). Of course, particle forces can have an indirect effect by influencing other terms in the balance equation.

The balance equation for $\overline{u_1^2}$ might be of most importance since production is directly contributed by the fluid Reynolds shear stress, $\overline{u_1 u_2}$, that is described by the mean momentum balance in the fluid. The transport of $\overline{u_1^2}$ in a statistically stationary case is given as

$$0 = \underbrace{-2\overline{u_1 u_2}\frac{\partial \overline{U}_1}{\partial x_2}}_{\text{Production}} \underbrace{-\frac{\partial}{\partial x_2}\overline{u_1^2 u_2}}_{\text{Turbulent transport}} \underbrace{-\frac{2}{\rho_f}\overline{u_1\frac{\partial p}{\partial x_1}}}_{\text{Velocity pressure-gradient correlation}} \underbrace{+\nu\frac{\partial^2}{\partial x_2^2}\overline{u_1^2}}_{\text{Viscous diffusion}} \underbrace{-2\nu\overline{\left(\frac{\partial u_1}{\partial x_k}\right)^2}}_{\text{Dissipation}} \underbrace{+2\overline{u_1 f_1}}_{\text{Velocity point-force correlation}}. \tag{20}$$

The transport equations of $\overline{u_2^2}$, $\overline{u_3^2}$ and $-\overline{u_1 u_2}$ are, respectively, given as

$$0 = -\frac{\partial}{\partial x_2}\overline{u_2^3} - \frac{2}{\rho_f}\overline{u_2\frac{\partial p}{\partial x_2}} + \nu\frac{\partial^2}{\partial x_2^2}\overline{u_2^2} - 2\nu\overline{\left(\frac{\partial u_2}{\partial x_k}\right)^2} + 2\overline{u_2 f_2}, \tag{21}$$

$$0 = -\frac{2}{\rho_f}\overline{u_3\frac{\partial p}{\partial x_3}} + \nu\frac{\partial^2}{\partial x_2^2}\overline{u_3^2} - 2\nu\overline{\left(\frac{\partial u_3}{\partial x_k}\right)^2} + 2\overline{u_3 f_3}, \tag{22}$$

$$0 = \overline{u_2^2}\frac{\partial \overline{U}_1}{\partial x_2} + \frac{\partial}{\partial x_2}\overline{u_1 u_2^2} + \frac{1}{\rho_f}\left(\overline{u_1\frac{\partial p}{\partial x_2}} + \overline{u_2\frac{\partial p}{\partial x_1}}\right) + \nu\frac{\partial^2}{\partial x_2^2}(-\overline{u_1 u_2}) + 2\nu\overline{\frac{\partial u_1}{\partial x_k}\frac{\partial u_2}{\partial x_k}} - \left(\overline{u_1 f_2} + \overline{u_2 f_1}\right) \tag{23}$$

4. Numerical method

4.1. Description of the DNS

The DNS of turbulent fluid flow in a channel is performed in a box with dimensions of $1900\nu/v_0^*$ in the streamwise direction (x_1), $300\nu/v_0^*$ in the wall-normal direction (x_2), and $950\nu/v_0^*$ in the spanwise direction (x_3). A pseudospectral fractional-step method (Lyons et al., 1991) is used for the spatiotemporal discretization. The feedback is calculated by using a first-order Euler explicit method. The computational grid is $128 \times 65 \times 128$. The resolutions in the streamwise and spanwise directions are $\Delta x_1^+ = 15$ and $\Delta x_3^+ = 7.4$, where the superscript plus represents a variable made dimensionless with v_0^* and ν. The resolutions in the wall-normal direction vary from $\Delta x_2^+ = 0.18$ at the wall to $\Delta x_2^+ = 7.4$ at the channel center. No slip boundary conditions are used at $x_2 = \pm H$ and periodicity is assumed in the x_1 and x_3 directions. The time step is $\Delta t^+ = 0.25$. The fluid

velocity seen by the particles is calculated using a mixed spectral-polynomial interpolation scheme developed by Kontomaris et al. (1992). The spatiotemporal resolution is the same as used by Lyons et al. (1991) to calculate single-phase turbulent flow.

4.2. Particle tracking

Displacements and velocities of the particles which do not collide with any particles during the time step are calculated by using a second-order Adams–Bashforth method. A first-order Euler explicit method is used for the times of injection and just after inter-particle collisions. Particles are removed from the field when they are at a distance of $d_p/2$ from a wall. Fluid velocities seen by particles in the next time step are obtained by interpolating the velocities obtained from the DNS, since we use explicit methods to calculate particle trajectories.

4.3. Calculation of statistics

Simulations were monitored by recording volume fractions, skin frictions and pressure drops. After confirming that these parameters stopped evolving and that both the fluid and solid phases were fully developed, calculations of statistics were continued until enough samples were recorded to capture the statistically stationary state. The convergence of the statistics is checked with (1) the mean wall-normal particle velocities, which should be zero at all x_2 in a statistically stationary state, and (2) the agreement between the calculated particle Reynolds shear stresses and Eq. (15). In the calculations, if $|\overline{V}_2^+| < 3 \times 10^{-4}$ at all x_2^+ (the criterion 1), the criterion 2 was satisfied. The duration that is needed to calculate the statistics varies with the volume fraction. Durations ranging from 2000 to $30,000 v/v_0^{*2}$ were used to calculate the statistics for volume fractions ranging from 1×10^{-5} (about 1500 particles in an instantaneous field) to 2.5×10^{-3} (about 375,000 particles in an instantaneous field).

The influence of changes in the computational grid and the size of the time step was not studied. Convergence of the calculation was checked with the criteria described above. In all calculations the momentum balance for the solid phase, as given by Eq. (15), was satisfied, so numerical momentum loss (or gain) related to the resolution (or due to dealiasing done in the DNS) is nearly zero at all x_2. In addition, the results shown in the next section capture many important aspects of laboratory measurements.

5. Results

5.1. Effect of feedback

The effects of feedback, without consideration of inter-particle collisions, are examined in this subsection. Before reviewing the results the mean particle Reynolds number is examined to check the validity of the use of the point force method. Fig. 2 presents the mean particle Reynolds numbers, $\overline{Re}_p = d_p^+[\boldsymbol{V}^+ - \boldsymbol{U}^+]$, for several

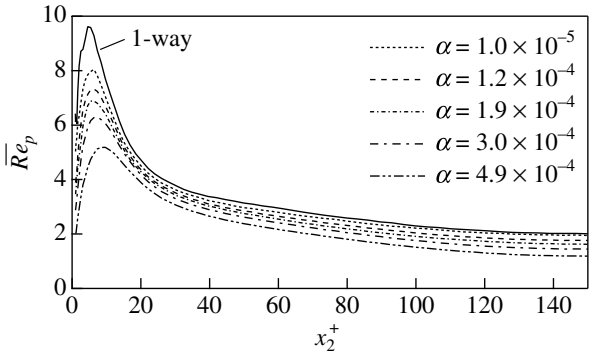

Fig. 2. Mean particle Reynolds numbers.

volume fractions. Values for the calculation in which feedback is not considered are also presented by the solid line. Similar results were obtained for other calculations in which elastic or inelastic collisions are considered in addition to feedback. The mean particle Reynolds number decreases with increasing volume fraction. It is small enough to be consistent with the use of the point force method. In the near-wall region ($x_2^+ \leqslant 20$) the mean particle Reynolds number is large because of the effect of injected particles, whose contribution decreases with increasing volume fraction.

Fig. 3 presents the mean velocities of the fluid and the solid phase in a statistically stationary state at $\alpha = 4.9 \times 10^{-4}$, which is the maximum volume fraction that could be realized in steady-state calculations that consider only feedback. Particles are, on average, lagging the fluid in the center region of the channel, $x_2^+ > 60$, and are, on average, leading the fluid in the near-wall region. This relation between $\overline{V}_1$ and $\overline{U}_1$ reflects the effects of particle inertia on wall-normal mixing. Similar relations are observed at different volume fractions. However, the differences between $\overline{V}_1$ and $\overline{U}_1$ decrease with increasing α because of the attenuation of the particle turbulence shown in Fig. 11.

The difference between $\overline{V}_1$ and $\overline{U}_1$ causes the mean streamwise point forces, $\overline{F}_1$, exerted on the fluid by particles shown in Fig. 4. In the center region, $x_2^+ > 60$, $\overline{F}_1$ is negative, so the fluid is decelerated by the particles. In the near-wall region, $x_2^+ < 60$, the particles accelerate the fluid. The magnitude of $\overline{F}_1$ increases with increasing α, that is, the concentration of point forces.

The friction velocity is obtained from the calculated fluid velocity gradient at the wall. Fig. 5a shows the mean fluid velocities made dimensionless with the actual friction velocities, v^*, for the statistically stationary cases in which 0.1, 1, 1.5, 2, 2.5 particles are injected from the wall over a computational time step. Changes in the friction velocity appear as changes in the bulk flow rate made dimensionless with v^* (since the dimensional volumetric flow is kept constant). The shapes of the mean fluid velocity profiles are seen to be almost unchanged with changes in particle concentration for $\alpha < 5 \times 10^{-4}$. The field becomes non-stationary and the volume fraction increases with time when the number of particles injected per time step is 2.6 or more.

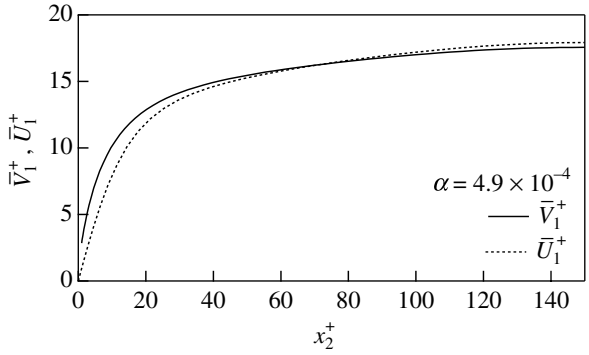

Fig. 3. Effect of feedback on the mean particle velocity and the mean fluid velocity at $\alpha = 4.9 \times 10^{-4}$.

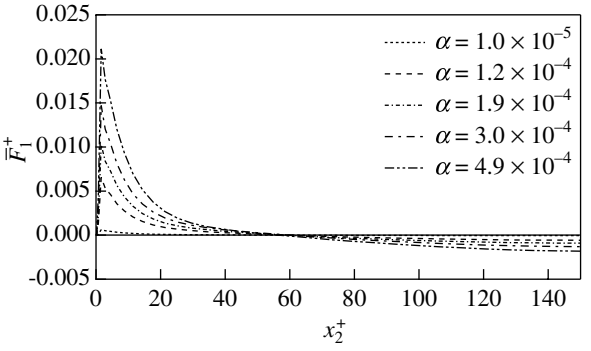

Fig. 4. Mean streamwise point forces.

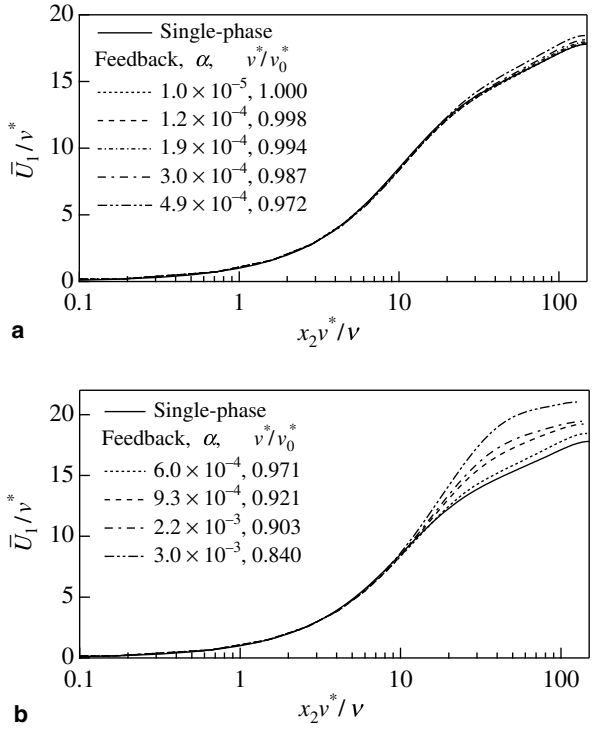

Fig. 5. Effect of feedback on the mean fluid velocity made dimensionless with the actual friction velocity. (a) Statistically stationary cases. (b) Time variation of the velocity profile and of α when 2.7 particles are injected per time step.

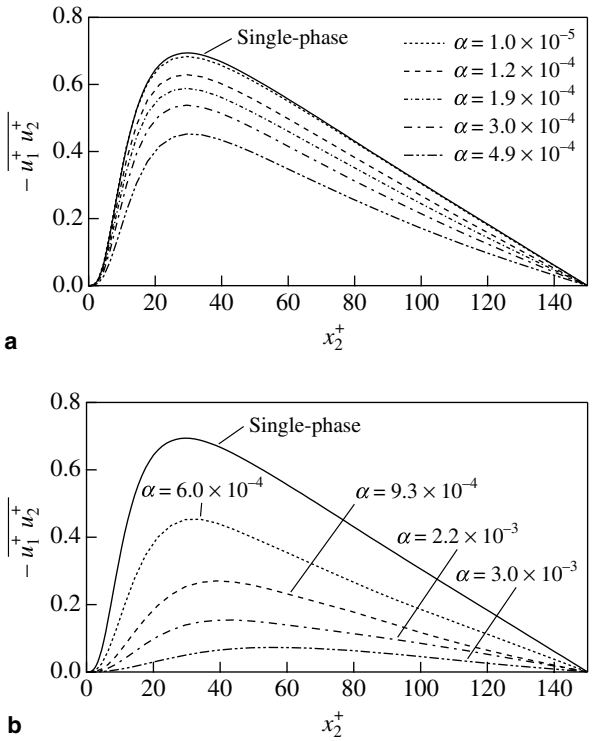

Fig. 6. Effect of feedback on the fluid Reynolds shear stress. (a) Statistically stationary cases. (b) Time variation when 2.7 particles are injected per time step.

Fig. 5b shows the changes in the dimensionless mean fluid velocity profile with increasing time when particles are injected at a rate of 2.7 per time step. The calculation was continued until $\alpha = 3 \times 10^{-3}$. The shape of the mean fluid velocity profile changes with increasing volume fraction for $\alpha >$ ca. 1×10^{-3}. The ratios of the actual friction velocity to the friction velocity for the single-phase flow are presented in the figures. Feedback is seen to have the effect of reducing the skin friction. This effect is of increasing importance with increasing α. It is noted that the changes in the skin friction are small in the range of α for which statistically stationary states can be realized.

Fig. 6 presents the fluid Reynolds shear stresses for the cases shown in Fig. 5. It is noted that the fluid Reynolds shear stress significantly decreases with increasing α for the stationary cases even when the change in the mean fluid velocity profile is not so large (see Fig. 5a). For the non-stationary case, the fluid Reynolds shear stress decreases drastically with increasing time and is seen to be approaching zero at all x_2.

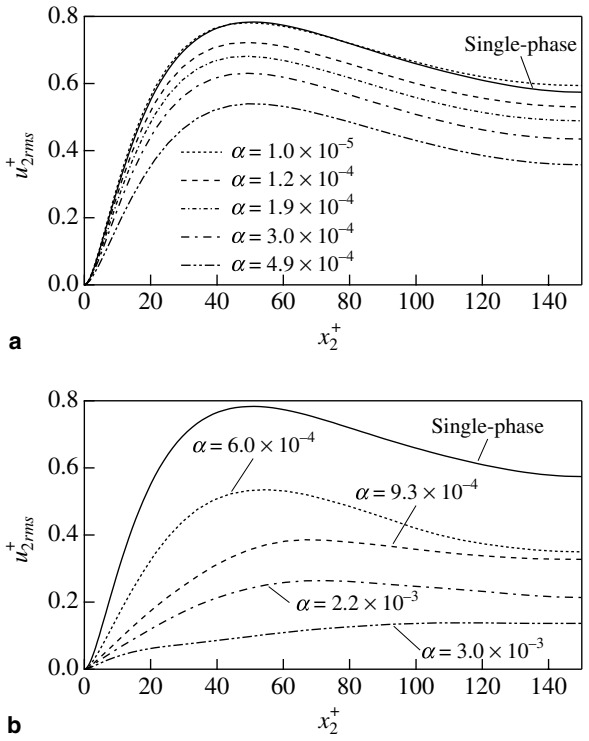

Fig. 7. Effect of feedback on the wall-normal fluid velocity fluctuation. (a) Statistically stationary cases. (b) Time variation when 2.7 particles are injected per time step.

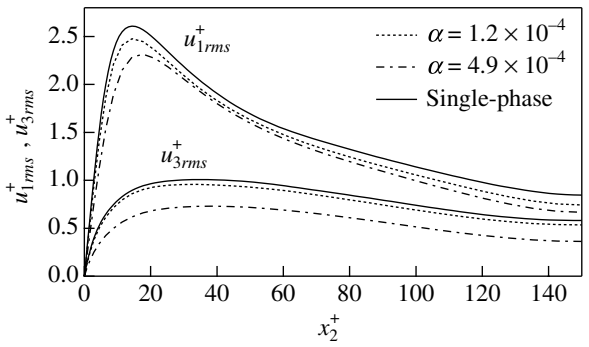

Fig. 8. Effect of feedback on the streamwise and spanwise fluid velocity fluctuations.

The root-mean-square value of the wall-normal fluid velocity fluctuations is attenuated with increasing α as shown in Fig. 7 for both the stationary and non-stationary cases. The drastic decreases in the fluid turbulence, observed at $\alpha > 10^{-3}$ for the non-stationary case, should be noted.

Attenuations of the streamwise and spanwise fluid velocity fluctuations are shown in Fig. 8. The per cent decrease in the streamwise fluid velocity fluctuations is not as large as observed for the other components. This is associated with increases in the spatial gradients of the mean fluid velocity with increasing α, shown in Fig. 5a at $20 < x_2^+ < 100$, even though the changes in the shape of the mean fluid velocity profile are seen to be small.

Instantaneous fluid fluctuating velocity fields in the center plane are presented in Fig. 9 for the single-phase flow, a statistically stationary case at $\alpha = 4.9 \times 10^{-4}$ and the non-stationary case at $\alpha = 3.0 \times 10^{-3}$. Dots represent locations of particles. (They do not represent the actual volume occupied by the particles.) Significant attenuation of the fluid turbulence is noted in Fig. 9b. The particles in the center plane are seen to be almost uniformly distributed and to be affecting all turbulent structures. The small-scale fluid turbulence is seen almost to vanish for the non-stationary case shown in Fig. 9c. The streamwise velocity fluctuations are seen to be banded. They cannot be characterized as turbulent. Clustering of particles is seen but the correlation between the clusters and the fluid velocity field is not obvious.

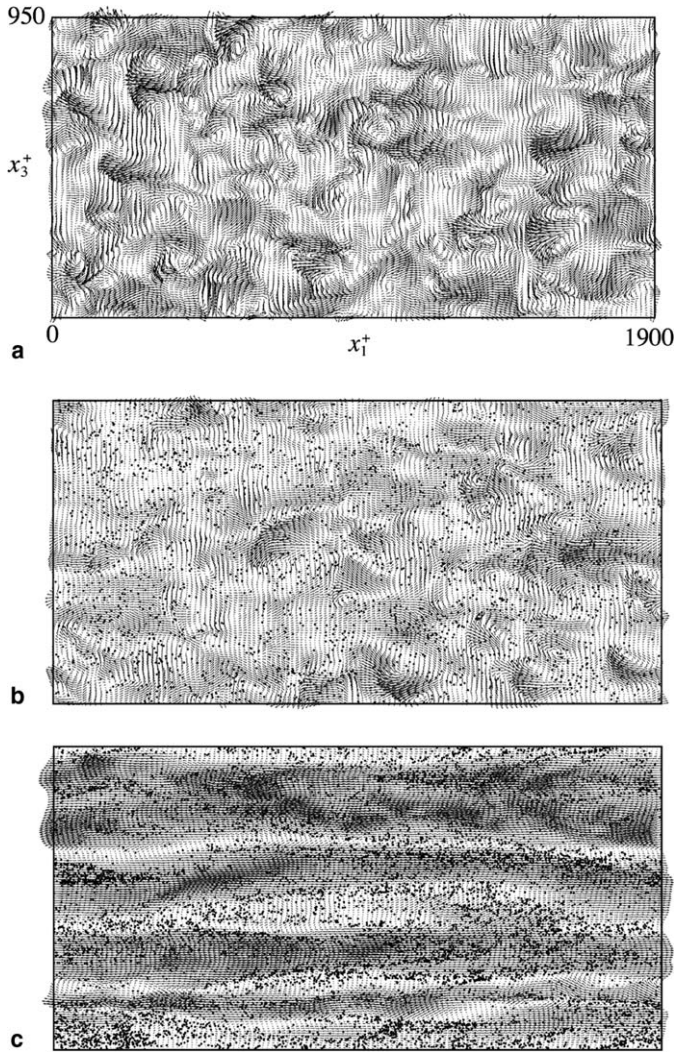

Fig. 9. Instantaneous fluid fluctuating velocity fields at the center plane. Dots represent locations of particles. Their sizes are magnified 5 times. (a) Single-phase flow. (b) A statistically stationary case at $\alpha = 4.9 \times 10^{-4}$. (c) A non-stationary case at $\alpha = 3.0 \times 10^{-3}$.

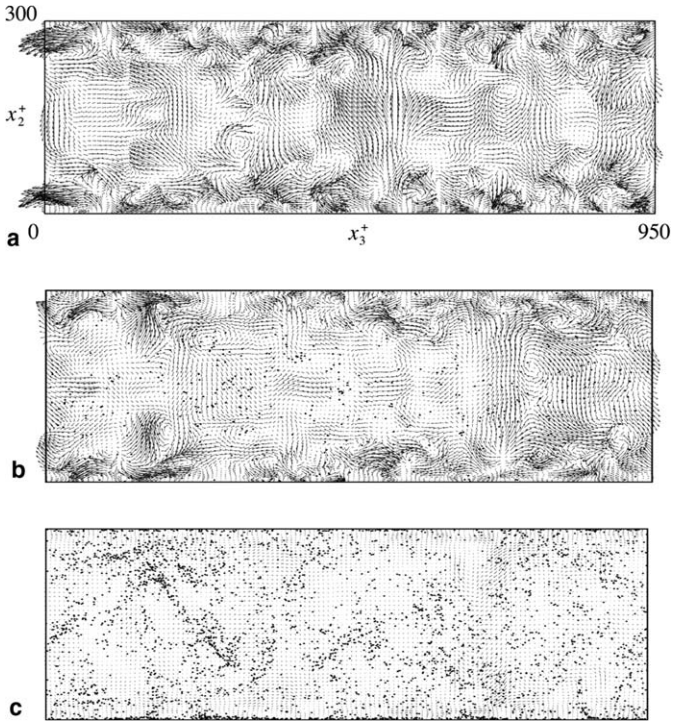

Fig. 10. Instantaneous fluid velocity fields in a cross section perpendicular to the direction of mean flow. Dots represent locations of particles. Their sizes are magnified 5 times. (a) Single-phase flow. (b) A statistically stationary case at $\alpha = 4.9 \times 10^{-4}$. (c) A non-stationary case at $\alpha = 3.0 \times 10^{-3}$.

Fig. 10 presents instantaneous fluid velocity fields in a cross section perpendicular to the direction of mean flow. A drastic attenuation of the longitudinal vortical structures near the wall with increasing α is clearly shown. The fluid turbulence has almost completely disappeared for the non-stationary field at $\alpha = 3.0 \times 10^{-3}$. Clustering of particles is seen in this cross section at this volume fraction.

The wall-normal particle velocity fluctuations for stationary cases are presented in Fig. 11. It is noted that the particle turbulence for the simulation with one-way coupling is much smaller than the fluid turbulence (shown in Fig. 7a at $x_2^+ > 20$) because the inertia of particles inhibits them from following the fluid turbulence (Reeks, 1977; Lee et al., 1989). It is larger than the fluid turbulence at $x_2^+ < 20$ because of the contribution of free-flight particles that move from the outer flow to the wall region (Brooke et al., 1994; Mito and Hanratty, 2004a). It decreases with increasing α because of the decrease in the fluid turbulence caused by feedback.

The product of the mean concentration and the cross correlation of v_1 and v_2 defines a mean momentum flux of the solid phase (see Eq. (14)) or the negative of a particle shear stress due to particle turbulence (see Eq.

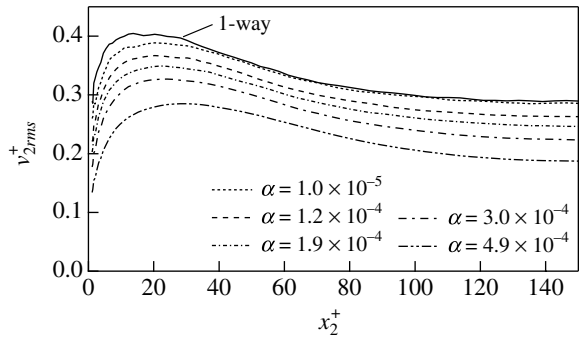

Fig. 11. Effect of feedback on the wall-normal particle velocity fluctuation.

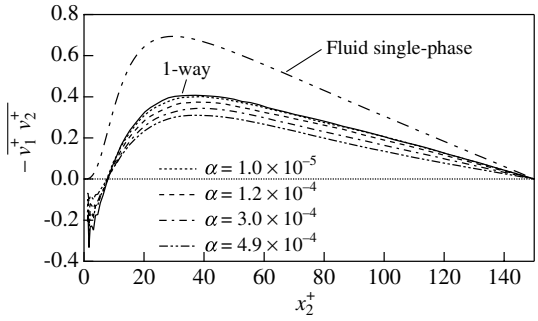

Fig. 12. Effect of feedback on the particle Reynolds shear stress.

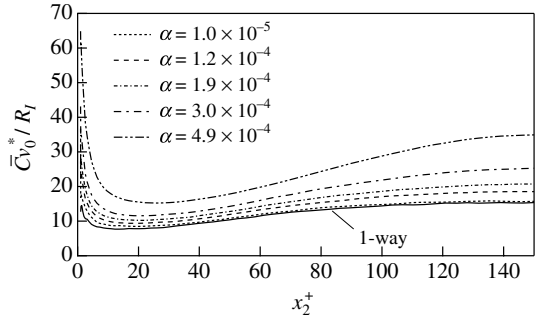

Fig. 13. Effect of feedback on the concentration profile.

(16)). The negative of the particle velocity correlation, $-\overline{v_1 v_2}$, obtained from calculations that include only feedback is presented in Fig. 12. The values for the one-way coupling simulation are smaller than the fluid Reynolds shear stresses for the single-phase flow because the inertia of the particles prevents them from following the fluid fluctuations. The correlation $-\overline{v_1 v_2}$ becomes negative at the wall because the particles are, on average, supplying streamwise momentum to the fluid (see Eq. (17)). The magnitude of the particle Reynolds stress decreases with increasing α as already seen for $v_{2\,\mathrm{rms}}$. However, $-\overline{C v_1 v_2}$ increases (see Fig. 13).

The concentration profiles of the particles for the statistically stationary cases, made dimensionless with the rate of injection, R_I, and the friction velocity when particles are not present, v_0^*, are presented in Fig. 13. The dimensionless concentration increases with increasing α at all x_2 because the decrease in the wall-normal particle turbulence is accompanied by a decrease in the deposition coefficient. An increase in the concentration with increasing the distance from the wall at $x_2^+ > 20$ is observed for all the cases considered. This is caused by turbophoresis (Caporaloni et al., 1975; Reeks, 1983) whereby particles tend to move from regions of high

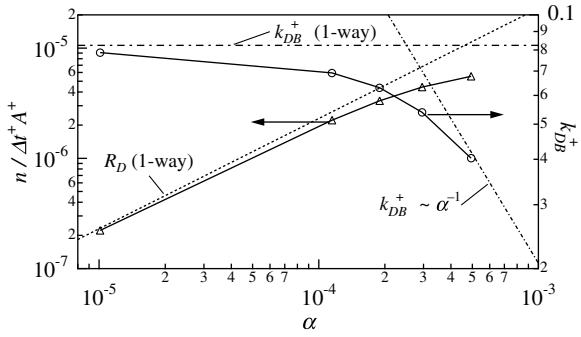

Fig. 14. Effect of feedback on the rate of deposition, $n/\Delta t^+ A^+$, and deposition coefficient, k_{DB}^+, varying with the volume fraction.

turbulence to regions of low turbulence. The accumulation of particles in the near-wall region occurs because the particles carried from the outer-region by free-flight get trapped or decelerated in the low turbulence region (Brooke et al., 1994). The large accumulation near the wall at $\alpha = 4.9 \times 10^{-4}$ reflects the small particle turbulence in the near-wall region, shown in Fig. 11.

Fig. 14 presents the rate of deposition for statistically stationary cases, for which R_D equals the rate of injection, $n/\Delta t^+ A^+$, where n is the number of particles injected from a wall per time step and A^+ is the dimensionless area of the wall. The deposition coefficient defined with $R_D = k_{DB}\rho_p\alpha$ is plotted in the dimensionless form $k_{DB}^+ = k_{DB}/v_0^*$. The values of R_D and k_{DB}^+ are also shown for the one-way coupling simulation, for which the effect of α on the fluid turbulence can be ignored. The feedback effect is evident at $\alpha > 10^{-5}$. The value of k_{DB}^+ is 50% of that for one-way coupling at $\alpha \approx 2 \times 10^{-4}$. The rate of deposition, R_D, is 50% of that for one-way coupling at $\alpha \approx 3 \times 10^{-4}$.

The asymptotic behavior of k_{DB}^+ at large α is defined with Eq. (1) as $k_{DB} = (R_I)_{MAX}/(\rho_p\alpha)$, where $(R_I)_{MAX}$ is the maximum value of R_I for which a statistically stationary state can be realized. In the flow system considered, $(R_I)_{MAX}$ occurs when the number of particles injected from a wall per time step is between 2.5 and 2.6. The value of 2.6 was used to test the proposed asymptotic behavior of $k_{DB}^+ \sim \alpha^{-1}$ shown in Fig. 14.

It is noted that the calculations in Fig. 14 show the same behavior as indicated in Fig. 1. The dimensionless rate of deposition, $n/\Delta t^+ A^+$, reaches a maximum value of approximately 6×10^{-6}. The dimensionless deposition coefficient, k_{DB}^+, is seen to show the asymptotic behavior of $k_{DB}^+ \sim \alpha^{-1}$ at $\alpha \approx 7 \times 10^{-4}$. Using the friction velocities measured in the laboratory measurements by Schadel et al. (1990) and by Andreussi (1983), $v^* = 3$–8 m/s, the maximum rate of deposition, shown in Fig. 14, can be calculated as a dimensional value within the range from 0.064 to 0.17 kg/m^{2}s. Both the maximum deposition rate and the volume fraction at which the rate of deposition reaches the maximum value appear to be slightly smaller than those shown in Fig. 1. The difference between the calculations and the laboratory measurements can be associated with particle interactions.

5.2. Effect of inter-particle collisions

This subsection considers the effect of collisions when there is no change in fluid turbulence. Two collision models are considered: (1) an elastic model with $e = 1$ and $\beta = -1$ (see Eqs. (6) and (7)) and (2) a highly inelastic model for which $e = 0.1$ and $\beta = 0$. The particles see the single-phase fluid turbulence since feedback is not considered. An investigation of the effects of e and β that uses a modified Langevin equation to calculate the fluid velocities seen by particles is presented in Appendix A. Only statistically stationary cases are considered in this subsection.

The ratios of the deposition coefficient, k_{DB}, to that for the one-way coupling simulation are presented in Fig. 15. An effect of elastic collisions on k_{DB} appears at $\alpha > 10^{-4}$. It is noted that elastic collisions increase k_{DB} because they increase particle turbulence. The inelastic collision model used in Fig. 15 is considered to be an extreme case (which might be characteristic of droplet interactions). Inelastic collisions are seen to decrease k_{DB}. However, the effect on k_{DB} is much smaller, in the range of α considered, than that associated with feedback (see Fig. 14). It is of interest to note the effect of inelastic collisions was found to be much greater when a

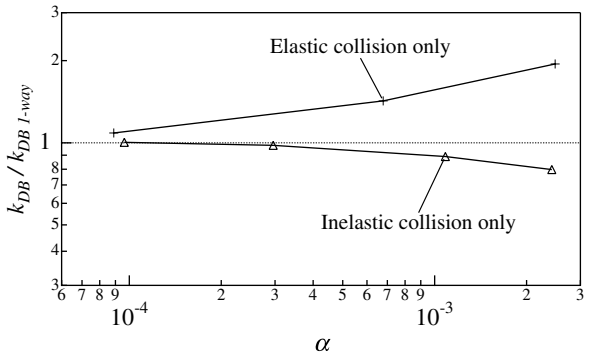

Fig. 15. Effect of inter-particle collisions on the deposition coefficient, varying with the volume fraction.

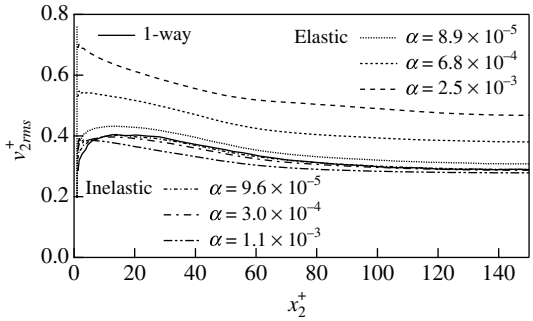

Fig. 16. Effect of inter-particle collisions on the wall-normal particle velocity fluctuation.

stochastic model that does not correctly capture small-scale turbulence is used. In fact a $k_{DB} \sim \alpha^{-1}$ relation is found at small α (see Appendix A).

Fig. 16 presents the wall-normal particle velocity fluctuations for the cases shown in Fig. 15. Elastic collisions cause the wall-normal turbulence to increase with increasing α (consistent with the increase in the deposition coefficient) because of the redistribution of particle turbulence among the v_1, v_2 and v_3 components. The particle turbulence decreases with increasing α when only inelastic collisions are occurring. However, the changes are much smaller than those observed in simulations that consider elastic collisions or feedback. Inelastic collisions attenuate all components of the particle turbulence (not shown).

5.3. Effect of feedback and inter-particle collisions

The combined effect of feedback and collisions is now discussed. When only feedback was considered decreases in fluid turbulence was accompanied by decreases in particle turbulence. This is associated with a decrease in the deposition coefficient and, therefore, an increase in particle concentration. This, in turn, increases the feedback, so a critical rate of injection exists beyond which a stationary state cannot be reached. Inelastic collisions decrease particle turbulence so, if anything, collisions should further decrease the deposition coefficient. Elastic collisions, however, increase particle turbulence, so increases in particle concentration need not lead to large decreases in the deposition coefficient. Stationary states are therefore reached for the entire range of injection rates that is considered.

Because the effect of the inelastic collisions is much smaller than the effect of feedback, simulations that considered both feedback and the inelastic collisions produced almost the same results as simulations that considered only feedback. Therefore, only calculations for elastic inter-particle collisions are considered for statistically stationary cases for which the rate of injection equals the rate of deposition.

Fig. 17 presents the mean velocities of the particles and of the fluid at $\alpha = 1.5 \times 10^{-3}$. As already seen in the calculation with only feedback, shown in Fig. 3, particles are, on average, leading the fluid in the near-wall

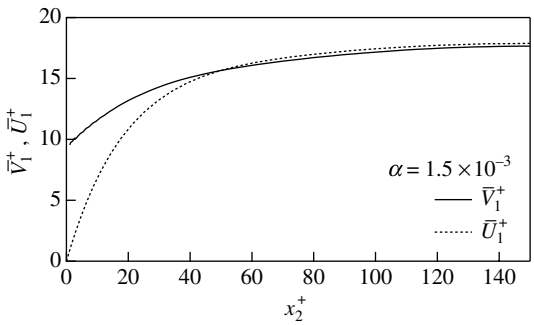

Fig. 17. Effect of feedback and elastic inter-particle collisions on the mean particle velocity and the mean fluid velocity at $\alpha = 1.5 \times 10^{-3}$.

region and are, on average, lagging the fluid in the center region. A large increase in the particle mean velocity in the near-wall region, which is caused by the large increase in the rate of injection, is noted.

Concentration profiles, $\overline{C}v_0^*/R_I$, calculated using both feedback and elastic inter-particle collisions are presented in Fig. 18. The dimensionless concentration increases with increasing rate of injection at $x_2^+ > 15$, but decreases at $x_2^+ < 15$.

The most striking results are the drastic attenuation of the fluid turbulence and the small change in particle turbulence with increasing α. Fig. 19a presents the wall-normal fluid velocity fluctuations for the cases shown in Fig. 18. Fig. 19b presents the fluid Reynolds shear stresses. At $\alpha = 1.5 \times 10^{-3}$, the fluid turbulence is seen to be completely damped and the fluid Reynolds shear stresses are nearly zero at all x_2^+.

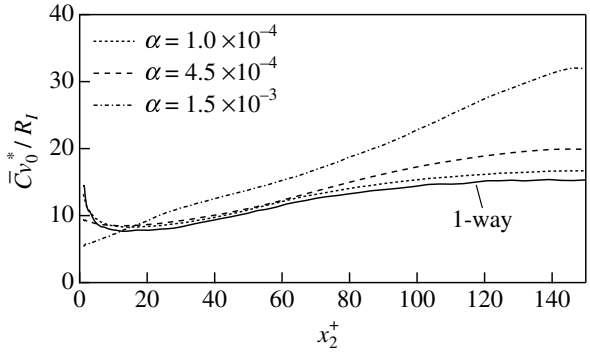

Fig. 18. Effect of feedback and elastic inter-particle collisions on the concentration profile.

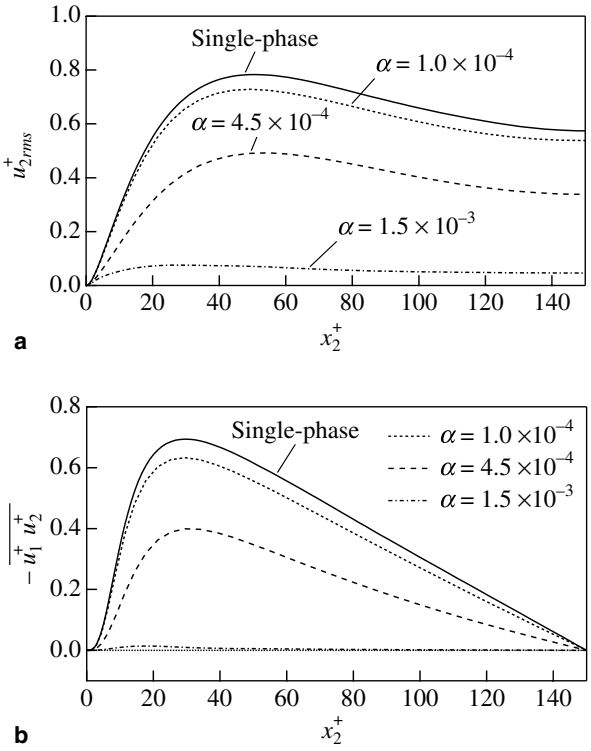

Fig. 19. Effect of feedback and elastic inter-particle collisions on the fluid turbulence. (a) Wall-normal velocity fluctuation. (b) Reynolds shear stress.

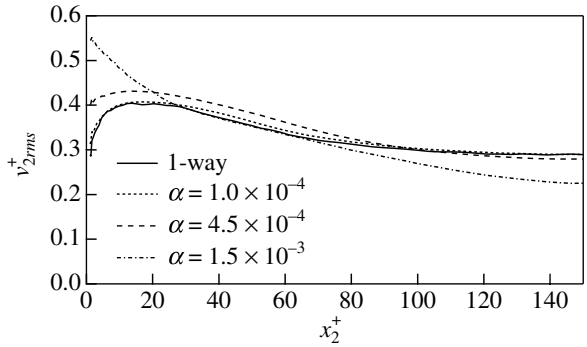

Fig. 20. Effect of feedback and elastic inter-particle collisions on the wall-normal particle velocity fluctuation.

The intensities of wall-normal particle velocity fluctuations are presented in Fig. 20. Surprisingly, the changes in the wall-normal particle turbulence with changing α are very small compared to the changes in the fluid turbulence. This occurs because the feedback effect which attenuates the wall-normal particle turbulence (by decreasing fluid turbulence) is counterbalanced by an increase caused by elastic collisions. The particle turbulence increases with increasing α in the near-wall region because of the increase in the rate of injection. (It is noted that particles are injected from a wall with the wall-normal velocity component of $1v_0^*$.) The magnitude of the gradient of the $v_{2\,\mathrm{rms}}$ increases with increasing α at $x_2^+ > 15$, so that the turbophoresis increases with increasing α. At $\alpha = 1.5 \times 10^{-3}$, the $v_{2\,\mathrm{rms}}$ is smaller in the center region than the value calculated for one-way coupling. Since the fluid turbulence at $\alpha = 1.5 \times 10^{-3}$, shown in Fig. 19a, is very small, the particle turbulence is considered to be mainly produced by elastic inter-particle collisions, which should be large close to the wall because of the contributions of injected particles.

The ratios of the deposition coefficients, calculated for the cases in which both feedback and inter-particle collisions are considered, compared to those calculated for one-way coupling, are presented in Fig. 21. The values for the calculations that considered only feedback are also presented. The deposition coefficients for the calculations with feedback and inelastic inter-particle collisions are nearly equal to those for the calculations with only feedback because of the relatively small effect of the inelastic collisions compared to the effect of feedback, shown in Fig. 15. Since the inelastic collisions have an effect of reducing the deposition coefficient, the deposition coefficients obtained from calculations with feedback and inelastic collisions are slightly smaller than those for the calculations with only feedback. The deposition coefficients obtained from calculations with feedback and elastic collisions are larger than those for the calculations with only feedback. This reflects the important contribution of elastic collisions to particle turbulence, shown in Fig. 15. It is noted that the changes in the deposition coefficients for $\alpha > 10^{-3}$ mainly reflect changes in particle turbulence caused by the elastic inter-particle collisions and are almost independent of fluid turbulence. Of interest is the possibility that the

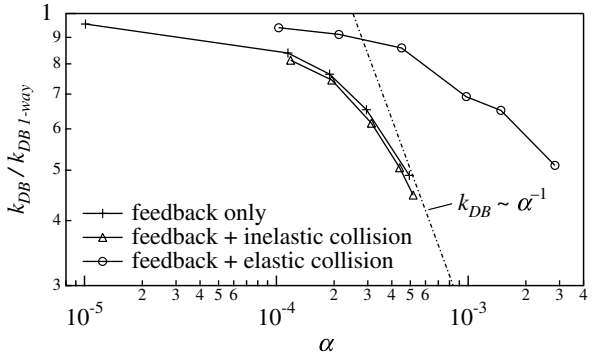

Fig. 21. Effect of feedback and inter-particle collisions on the deposition coefficient, varying with the volume fraction.

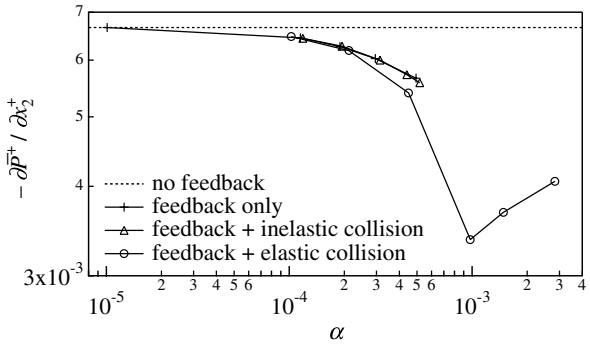

Fig. 22. Effect of feedback and inter-particle collisions on the mean pressure gradient, varying with the volume fraction.

deposition coefficient calculated with feedback and elastic collisions might continue to decrease with increasing α and eventually show an α^{-1} behavior. However, calculations at such large volume fractions are not easily executed with a DNS.

The laboratory measurements in Fig. 1 show that the rate of deposition is roughly constant at large α, where $k_{\mathrm{DB}} \sim \alpha^{-1}$. Fig. 21 shows that this behavior is realized for the calculation with feedback and inelastic inter-particle collisions. However, it appears at a slightly smaller α than is observed in Fig. 1 as pointed out in the comparison between the calculations that considered only feedback, shown in Fig. 14, and the laboratory measurements. This behavior is not realized in the region of $\alpha < 4 \times 10^{-3}$ for the calculation with feedback and elastic inter-particle collisions. The use of an elastic inter-particle collision model does not produce the tendency observed in laboratory studies of gas–liquid annular flows. Thus we suggest that an inelastic inter-particle collision model which represents an intermediate inelasticity between the elastic and inelastic models, considered in this study, might better capture the asymptotic behavior.

Fig. 22 presents the dimensionless mean pressure gradients obtained from calculations that consider feedback. The mean pressure drop for the single-phase flow, which is equal to the pressure drop for the flows without feedback, is denoted by the dashed line. As shown in Eq. (11) the mean pressure drop contains positive contributions from the fluid resisting stress of the wall, $\bar{\tau}_{\mathrm{W}}$, and negative contributions from the bulk mean point force, $F_{1\mathrm{B}}$. As shown in Eq. (18) the latter may be looked upon as resulting from the net exchange of momentum to the wall due to injected and depositing particles. The pressure drop decreases with increasing α at $10^{-4} < \alpha < 1 \times 10^{-3}$ mainly because of the increases in $F_{1\mathrm{B}}$, which represents momentum supplied to the fluid by solid particles, as shown in Eq. (17). At very large α the fluid turbulence is close to zero so the fluid velocity is given by Eq. (10) with $\overline{u_1 u_2} = 0$. The solution of this equation gives the fluid velocity profile and $\bar{\tau}_{\mathrm{W}}$. The latter will increase with increasing α, as indicated in Fig. 22 for $\alpha > 1 \times 10^{-3}$. This accounts for the increase in $-\partial\overline{P}^+/\partial x_2^+$ with increasing α shown in Fig. 22 for large α.

6. Fluid momentum and energy balances for the fluid

6.1. Motivation

Some understanding of the role of feedback in decreasing fluid turbulence can be obtained by considering momentum and energy balances for the fluid.

6.2. Momentum balance for the fluid, considering only feedback

The terms in Eq. (10) made dimensionless with ρ_{f}, v_0^* and ν are presented in Fig. 23a for $\alpha = 1.2 \times 10^{-4}$ and in Fig. 23b for $\alpha = 4.9 \times 10^{-4}$. The contribution of the pressure gradient, represented by $-(\partial\overline{P}^+/\partial x_1^+)(H^+ - x_2^+)$ is the left side of Eq. (10). It equals the sum of the contributions from the Reynolds stress, $-\overline{u_1^+ u_2^+}$, the viscous stress, $\partial\overline{U}_1^+/\partial x_2^+$, and the negative of the particle forces on the fluid (or the force of the fluid on the solids) in the region between x_2^+ to H^+, $-\int_{x_2^+}^{H^+} \overline{F}_1^+ \, \mathrm{d}x_2^+$, which is equal to $-(\overline{C}/\rho_{\mathrm{f}})\overline{v_1^+ v_2^+}$ (see Eq. (15)).

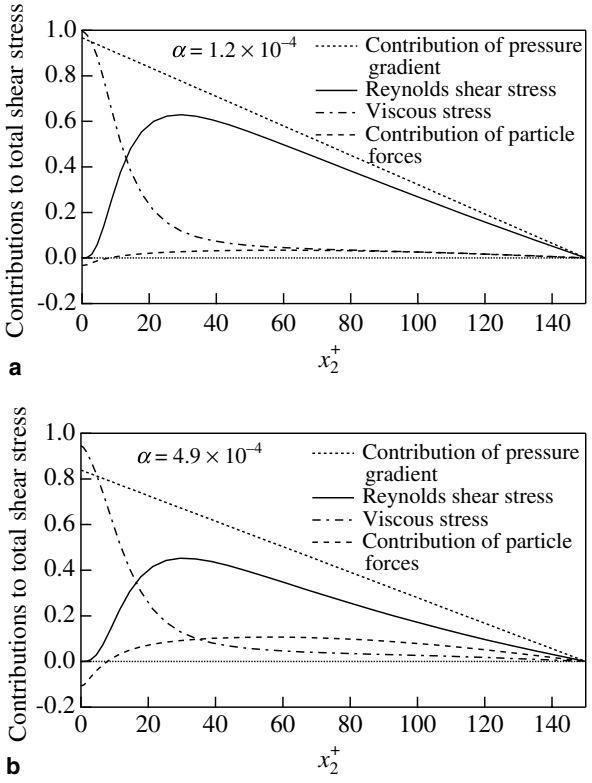

Fig. 23. Effect of feedback on the fluid momentum balance. (a) $\alpha = 1.2 \times 10^{-4}$. (b) $\alpha = 4.9 \times 10^{-4}$.

For a single-phase flow the contribution of the pressure gradient is unity at $x_2^+ = 0$. It is noted that the Reynolds stress for the fluid is smaller when particles are present. This arises partly because the pressure gradient decreases and more importantly because the net force of the particles on the fluid in the region between x_2 and H partially balances the force due to pressure gradient, so that smaller values of the Reynolds stress are needed to balance the pressure-gradient forces. Thus, the fluid Reynolds shear stresses decrease to accommodate the contribution due to particle forces.

In considering the contributions to the fluid Reynolds shear stress, it might be useful to use a balance equation for the fluid Reynolds shear stress, which is derived using Eqs. (16) and (18) as

$$-\rho_f \overline{u_1 u_2} = \underbrace{\left[\frac{H - x_2}{H}\bar{\tau}_W - \mu\frac{\partial \overline{U}_1}{\partial x_2}\right]}_{\text{Viscous shear stresses}} + \underbrace{\left[\overline{C}\overline{v_1 v_2} - \frac{H - x_2}{H}\overline{C}_W(\overline{v_1 v_2})_W\right]}_{\text{Particle forces}}. \tag{24}$$

Thus the fluid Reynolds stress is represented as the resultant of the viscous shear stress and the stress exerted by particles. With this consideration, the large decrease in the fluid Reynolds shear stress at $\alpha = 4.9 \times 10^{-4}$ is seen to be caused mainly by the large increase in the particle forces, that is, the volume fraction, because the difference between $\overline{V}_1$ and $\overline{U}_1$ decreases with increasing α.

6.3. Energy balance equation for the fluid, considering only feedback

A striking effect of feedback is the decrease in fluid turbulence. Therefore, it is of interest to consider the balance equation for $\overline{u_1^2}$, Eq. (20). The only term representing a direct effect of the particles on the fluid turbulence is velocity-point force correlation $2\overline{u_1 f_1}$, where f_1 is a component of the fluctuations in the point force. The dominant term in Eq. (20) is the production, $-2\overline{u_1 u_2}(\partial \overline{U}_1/\partial x_2)$.

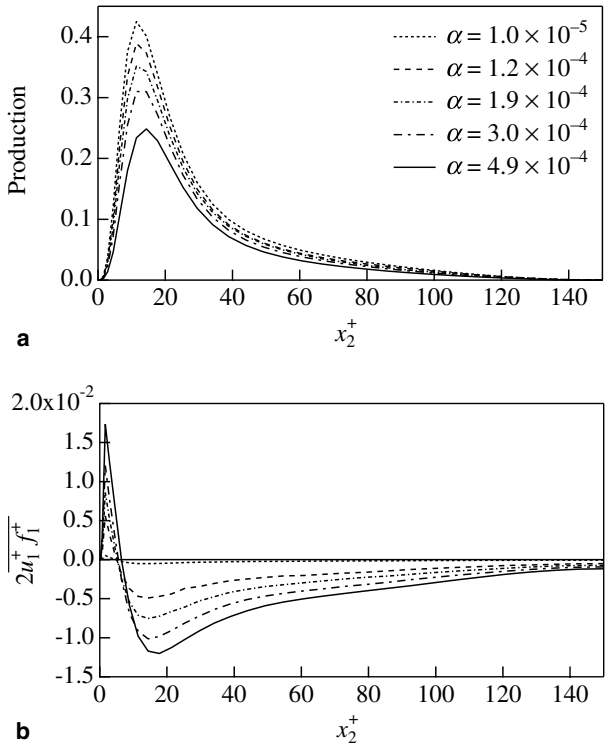

Fig. 24. Effect of feedback on the energy balance for $\overline{u_1^2}$. (a) Production. (b) Velocity-point force correlation.

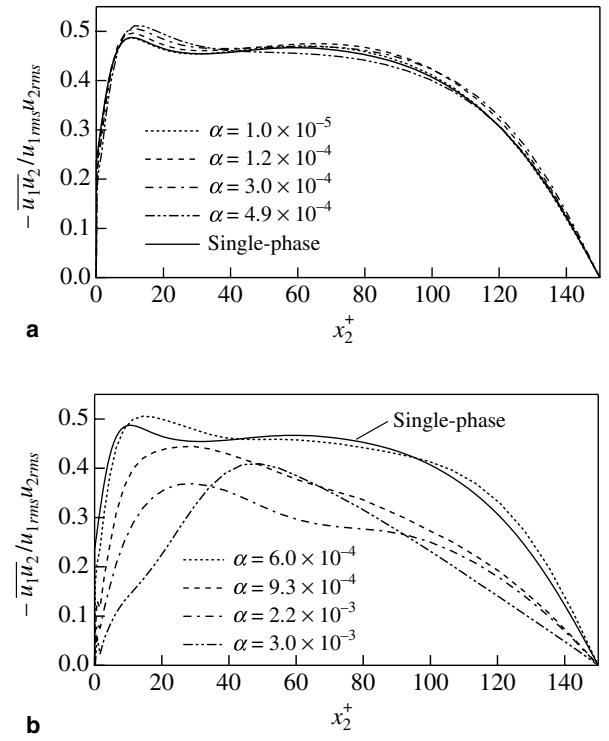

Fig. 25. Effect of feedback on the correlation coefficient of the fluid velocity fluctuations. (a) Statistically stationary cases. (b) Time variation in a non-stationary case.

Fig. 24a presents calculated profiles of the production, made dimensionless with v_0^* and v. It is noted that this decreases with increasing α because of the decrease in the fluid Reynolds shear stress. Similar plots are presented in Fig. 24b for the dimensionless velocity-point force correlation. It is seen from Eq. (20) that positive values of this quantity have the effect of increasing $\overline{u_1^2}$; negative values cause a decrease in $\overline{u_1^2}$. From Fig. 24b it is seen that the velocity-point force correlation should cause a decrease in $\overline{u_1^2}$. However, Fig. 24 shows that the production terms are an order of magnitude larger than the velocity-point force correlation so the effect of particles on fluid turbulence is mainly caused by decreases in the Reynolds shear stress.

The correlation coefficients, $-\overline{u_1 u_2}/u_{1\,\mathrm{rms}} u_{2\,\mathrm{rms}}$, for the calculations with only feedback are presented in Fig. 25 for both stationary and non-stationary cases. The correlation coefficients for the stationary cases shown in Fig. 25a with $\alpha < 5 \times 10^{-4}$ are almost the same as what is found for single-phase flows. For the non-stationary case shown in Fig. 25b, large changes in the correlation coefficient appear at $\alpha > 9 \times 10^{-4}$. These are reflected in the dramatic changes in the instantaneous velocity fields shown in Figs. 9 and 10.

7. Concluding remarks

As pointed out in Section 1 and in Fig. 1, droplet deposition measurements in gas–liquid annular flows show a remarkably large decrease in the deposition rate coefficient at relatively small volume fractions. Results from this paper suggest that point forces of particles on a fluid, due to a slip, cause decreases in fluid turbulence. The particle turbulence (and, therefore, the deposition coefficient) changes with fluid turbulence, but particle turbulence is also affected by droplet collisions. Elastic collisions enhance particle turbulence and at large enough volume concentrations could be controlling.

When drops interact they distort. This leads to inelastic effects and, in particular, could reduce the relative tangential motion of two colliding particles to zero. These inelastic collisions have the effect of reducing particle turbulence.

Thus, the decrease in the deposition coefficient in annular flow can be explained by a change in fluid turbulence caused by the presence of particles and by droplet collisions which are inelastic. Calculations based on this model are remarkably close to experimental data presented in Fig. 1.

The study supports previous work by Li et al. (2001) which shows that calculations in a DNS based on the point force method can predict large changes in fluid turbulence. Similar calculations in an LES (Yamamoto et al., 2001; Segura et al., 2004) produced much smaller degradation of fluid turbulence than indicated by experiments. Furthermore, we have found that calculations in which fluid turbulence is represented with a stochastic model fail to capture the effect of inelastic collisions. Both of these results suggest that it is necessary to represent accurately small-scale turbulence.

The system considered in this paper differs from other studies in a number of ways: The main focus is on particle turbulence and particle deposition. Particles are removed from the system when they strike a wall. Thus particle bouncing from the wall is not considered. Interactions of droplets are usually different from interactions of solid particles in that they are inelastic and might be represented by a model which does not allow tangential slip. Because the injected particles have a larger velocity than the depositing particles there is a net momentum transfer from the wall. This makes a negative contribution to the pressure gradient, so decreases in the pressure drop can be realized.

The widely quoted experimental studies of downward flow of a suspension of spheres in a channel by Eaton and his coworkers (Kulick et al., 1994; Paris and Eaton, 2001) involves a situation in which particles striking the wall have a higher velocity than particles rebounding from the wall. Thus, there is a net momentum transfer to the wall due to the particle–wall interaction. This can lead to an increase in the pressure drop. A number of their experiments with particle inertial time constants of $\tau_p^+ = 300, 2100, 2600$ showed decreases in the fluid turbulence energy similar to what is observed in this study. This suggests that the mechanism for the reducing the fluid turbulence could be the same as what has been observed in our study. Some support for this can be obtained from a consideration of the momentum balance (see Eqs. (10) and (24) and Fig. 23). For both cases, the point force contributions give rise to a decrease in the Reynolds shear stress needed to satisfy conservation of momentum. This, in turn, leads to a decrease in the production of fluid turbulence.

It is of interest to note that the observed influence of point forces on fluid turbulence has a kinship to findings on polymer drag reduction. Here polymer molecules (or aggregates) create local stresses in the turbulence and the Reynolds shear stresses decrease to accommodate these polymer stresses (Warholic et al., 1999).

Acknowledgements

This work is supported by DOE under grant DEFG02-86ER 13556. Computer resources have been provided by the National Center for Supercomputing Applications located at the University of Illinois.

Appendix A. Test of inter-particle collision models using a stochastic simulation

For cases in which the feedback effect is not considered, a modified Langevin equation can be used to provide a stochastic representation of fluid velocity fluctuations seen by a particle (Mito and Hanratty, 2003). This approach was used to examine the effects of various types of inter-particle collision models.

Jointly Gaussian random variables which correctly give all of the second moments of the fluid velocity fluctuations are used for the forcing functions. The mean velocities of the fluid and the statistics of the turbulence that appear in the model were obtained from a DNS (Mito and Hanratty, 2002). We follow the simple approach, described by Mito and Hanratty (2003), that uses the time constants characterizing the dispersion of fluid particles to define the time constants in the model.

Displacements and velocities of particles are calculated using the method described in Section 4.2. The modified Langevin equation is solved by using a fully implicit method in order to specify the fluid velocities.

The elastic inter-particle collision model, characterized by $e = 1$ and $\beta = -1$ in Eqs. (7) and (8), and several inelastic inter-particle collision models, characterized by $e = 0$, 0.1, 0.4, 0.7, 1 and $\beta = 0$, are considered. The use of the stochastic simulation enabled us to investigate effects of a large range of e for the inelastic collision model with $\beta = 0$ and effects of α ranging from 7×10^{-6} to 2×10^{-2} for each inter-particle collision model.

Fig. 26 presents dimensionless deposition coefficients, k_{DB}^{+}, calculated with the elastic collision model and several inelastic collision models. The deposition coefficients, obtained in the calculations with a DNS to simulate fluid velocities seen by particles, in which feedback is not taken into account, shown in Fig. 20, are also presented by the filled symbols. The deposition coefficients for one-way coupling are presented for both calculations with the modified Langevin equation and with the DNS. Comparisons between the calculations with the modified Langevin equation and with the DNS can be done by using their results for the elastic collisions and for the inelastic collisions with $e = 0.1$. They lead to the conclusion that the model can qualitatively capture the behaviors that were observed with the DNS when the elastic collisions were considered and that the error increases with increasing α and when the inelastic collisions are considered. These errors are caused because the Langevin equation cannot represent small-scale fluid turbulence correctly; that is, particles in a small volume see uncorrelated fluid velocity fluctuations. Because particles tend to cluster when they undergo

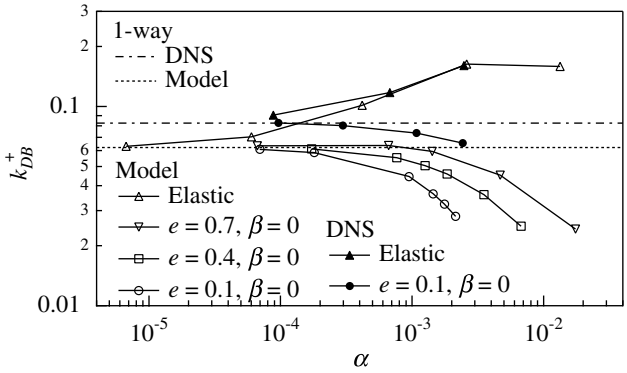

Fig. 26. Effect of inter-particle collisions on the deposition coefficient, varying with the volume fraction. A modified Langevin equation is used to calculate fluid velocity fluctuations seen by a particle.

inelastic collisions, the error increases for the calculation with the inelastic collisions. Thus the results obtained with this approach are only used to obtain a qualitative representation of behavior when inter-particle collisions are considered.

Elastic collisions are seen to cause an increase in the deposition coefficient. With the assumption of $\beta = 0$ (Campbell and Brennen, 1985), the deposition coefficient is seen to display the non-linear behavior, $k_{DB} \sim \alpha^{-1}$, at $\alpha > 4 \times 10^{-4}$ for $e = 0.1$. The inter-particle collision models used in the present study with a DNS representation of fluid turbulence were selected by a consideration of this result.

References

Andreussi, P., 1983. Droplet transfer in two-phase annular flow. Int. J. Multiphase Flow 9, 697–713.

Andreussi, P., Zanelli, S., 1976. Liquid phase mass transfer in annular two-phase flow. Ingegn. Chim. 12, 132–136.

Brooke, J.W., Hanratty, T.J., McLaughlin, J.B., 1994. Free-flight mixing and deposition of aerosols. Phys. Fluids 6, 3404–3415.

Campbell, C.S., Brennen, C.E., 1985. Computer simulation of granular shear flows. J. Fluid Mech. 151, 167–188.

Caporaloni, M., Tampieri, F., Trombetti, F., Vittori, O., 1975. Transfer of particles in nonisotropic air turbulence. J. Atmos. Sci. 32, 565–568.

Chen, M., Kontomaris, K., McLaughlin, J.B., 1998. Direct numerical simulation of droplet collisions in a turbulent channel flow. Part I: collision algorithm. Int. J. Multiphase Flow 24, 1079–1103.

Crowe, C.T., Sharma, M.P., Stock, D.E., 1977. The particle-source-in cell (PSI-CELL) model for gas-droplet flows. J. Fluids Eng. 99, 325–332.

Elghobashi, S., Truesdell, G.C., 1993. On the two-way interaction between homogeneous turbulence and dispersed solid particles. I: turbulence modification. Phys. Fluids A 5, 1790–1801.

Govan, A.H., Hewitt, G.H., Owen, D.G., Bott, T.R., 1988. An improved CHF modelling code. Presented at the Second UK National Heat Transfer Conference, Strathclyde University, Glasgow.

Hay, K.J., Liu, Z.C., Hanratty, T.J., 1996. Relation of deposition to drop size when the rate law is nonlinear. Int. J. Multiphase Flow 22, 829–848.

Kontomaris, K., Hanratty, T.J., McLaughlin, J.B., 1992. An algorithm for tracking fluid particles in a spectral simulation of turbulent channel flow. J. Comput. Phys. 103, 231–242.

Kulick, J.D., Fessler, J.R., Eaton, J.K., 1994. Particle response and turbulence modification in fully developed channel flow. J. Fluid Mech. 277, 109–134.

Lee, M.M., Hanratty, T.J., Adrian, R.J., 1989. The interpretation of droplet deposition measurements with a diffusion model. Int. J. Multiphase Flow 15, 459–469.

Li, Y., McLaughlin, J.B., Kontomaris, K., Portela, L., 2001. Numerical simulation of particle-laden turbulent channel flow. Phys. Fluids 13, 2957–2967.

Lun, C.K.K., Liu, H.S., 1997. Numerical simulation of dilute turbulent gas–solid flows in horizontal channels. Int. J. Multiphase Flow 23, 575–605.

Lun, C.K.K., Savage, S.B., 1987. A simple kinetic theory for granular flow of rough, inelastic, spherical particles. J. Appl. Mech. 54, 47–53.

Lyons, S.L., Hanratty, T.J., McLaughlin, J.B., 1991. Large scale computer simulation of fully developed turbulent channel flow with heat transfer. Int. J. Num. Methods Fluids 13, 999–1028.

Mito, Y., Hanratty, T.J., 2002. Use of a modified Langevin equation to describe turbulent dispersion of fluid particles in a channel flow. Flow Turbul. Combust. 68, 1–26.

Mito, Y., Hanratty, T.J., 2003. A stochastic description of wall sources in a turbulent field. Part 1: verification. Int. J. Multiphase Flow 29, 1373–1394.

Mito, Y., Hanratty, T.J., 2004a. A stochastic description of wall sources in a turbulent field. Part 2: calculation for a simplified model of horizontal annular flows. Int. J. Multiphase Flow 30, 803–825.

Mito, Y., Hanratty, T.J., 2004b. Concentration profiles in a turbulent suspension when gravity is not affecting deposition. Int. J. Multiphase Flow 30, 1311–1336.

Namie, S., Ueda, T., 1972. Droplet transfer in two-phase annular mist flow. Part 1: experiment of droplet transfer rate and distributions. Bull. JSME 15, 1568–1580.

Oesterle, B., Petitjean, A., 1993. Simulation of particle-to-particle interactions in gas–solid flows. Int. J. Multiphase Flow 19, 199–211.

Pan, Y., Banerjee, S., 1996. Numerical simulation of particle interactions with wall turbulence. Phys. Fluids 8, 2733–2755.

Paris, A.D., Eaton, J.K., 2001. Turbulence attenuation in a particle-laden channel flow. TSD-137, Stanford University, CA.

Reeks, M.W., 1977. On the dispersion of small particles suspended in an isotropic turbulent field. J. Fluid Mech. 83, 529–546.

Reeks, M.W., 1983. The transport of discrete particles in inhomogeneous turbulence. J. Aerosol Sci. 14, 729–739.

Schadel, S.A., Leman, G.W., Binder, J.L., Hanratty, T.J., 1990. Rates of atomization and deposition in vertical annular flow. Int. J. Multiphase Flow 16, 363–374.

Segura, J.C., Eaton, J.K., Oefelein, J.C., 2004. Predictive capabilities of particle-laden large eddy simulation. TSD-156, Stanford University, CA.

Sommerfeld, M., 2001. Validation of a stochastic Lagrangian modelling approach for inter-particle collisions in homogeneous isotropic turbulence. Int. J. Multiphase Flow 27, 1829–1858.

Squire, K.D., Eaton, J.K., 1990. Particle response and turbulence modification in isotropic turbulence. Phys. Fluids A 2, 1191–1203.

Tanaka, T., Tsuji, Y., 1991. Numerical simulation of gas–solid two-phase flow in a vertical pipe: on the effect of inter-particle collision. Gas–Solid Flows, FED-Vol. 121. ASME, pp. 123–128.

Teixeira, J.C., Azzopardi, B.J., Bott, T.R., 1987. The effect of inserts in drop sizes in vertical annular flow. UKAEA Report AERE R12641.

Warholic, M.D., Massah, H., Hanratty, T.J., 1999. Influence of drag-reducing polymers on turbulence: effects of Reynolds number, concentration and mixing. Exp. Fluids 27, 461–472.

Woodmansee, D.E., Hanratty, T.J., 1969. Mechanism for the removal of droplets from a liquid surface by a parallel air flow. Chem. Eng. Sci. 24, 299–307.

Yamamoto, Y., Potthoff, M., Tanaka, T., Kajishima, T., Tsuji, Y., 2001. Large-eddy simulation of turbulent gas-particle flow in a vertical channel: effect of considering inter-particle collisions. J. Fluid Mech. 442, 303–334.